

Measurement and processing of scattered ultrawide-band/short-pulse signals

Edward Rothwell, Kun-Mu Chen, Dennis Nyquist, John Ross, and Robert Bebermeyer

Department of Electrical Engineering, Michigan State University
East Lansing, MI 48824

ABSTRACT

High quality ultrawide-band measurements provide a basis for understanding the transient scattering phenomena necessary for the development of short-pulse radar target identification and detection schemes. This paper describes several techniques used at Michigan State University (MSU) for the acquisition, processing and interpretation of ultra-wideband scattering data. By performing measurements over a sufficiently large bandwidth, the early-time specular nature of a radar target and the late-time resonant behavior can be observed simultaneously within a single target signature. Special attention has been given at MSU to enhancing the equivalent bandwidth of the measurement system through a spectral splicing and extrapolation method. Observation and interpretation of the various scattering phenomena and their dependence on target aspect are then interpreted through several visualization techniques, including scattering plots, frequency-time plots and images.

Key words -- impulse radar, ultrawide-band radar, electromagnetic scattering measurements

1. INTRODUCTION

The development of viable short-pulse radar target identification systems¹ has prompted a need for understanding the basic phenomena of transient electromagnetic scattering from realistic targets. This is most easily accomplished through laboratory measurements over ultrawide frequency bandwidths. If the bandwidth is large enough, a target signature can be measured which contains both the early-time specular target response (a high frequency effect), and the late-time natural resonance response (a low frequency effect). Each of these components has been suggested for use in target identification schemes², and with sufficient bandwidth both could be used in a single technique³.

A scattering range has been developed at Michigan State University (MSU) which allows calibrated measurements of the near backscattering properties of scale model targets over the effective frequency range of 0-18 GHz for all linear polarization combinations (hh, hv, vh, vv). The bandwidth is achieved through a combination of frequency scaling, splicing and extrapolation techniques which employ a genetic algorithm to enforce the causality of the equivalent time-domain signature. Details of the bandwidth enhancement are given in Section 2, along with a description of the range calibration technique. A computer controlled target rotator capable of a positioning accuracy of 0.15° allows a detailed study of the variation of target scattering as a function of aspect angle. The wide bandwidth combined with the fine angular resolution of the measurements results in a large amount of data for each target, the physical interpretation of which is facilitated by various visualization techniques. Several methods for visualizing the data are presented in Section 3, including scattering plots, frequency-time plots, and imaging based on physical optics. Images and scattering plots are useful for interpreting the early-time specular behavior of targets as a function of aspect angle, while frequency-time plots allow the identification of such interesting physical phenomena as the resonance of target substructures. The late-time behavior is described best through plots of the aspect variation of the late-time modal amplitudes.

2. MEASUREMENT TECHNIQUES

The free-field scattering measurement system at MSU is a swept-frequency system utilizing a Hewlett-Packard HP-8720B vector network analyzer. While the network analyzer is capable of performing measurements over the band 0.13-20 GHz, the practical measurement band is controlled by the rated antenna bandwidth. Two sets of TEM horn antennas are available for use, American Electronic Laboratories model AEL H-1734 (0.5-6 GHz rated bandwidth) and AEL-1498 (2-18 GHz). The first set of antennas is combined with a Picosecond Pulse Labs broadband amplifier (11 dB gain) to give a viable 0.4-7 GHz measurement band, while the second set of antennas is combined with a Hewlett Packard HP-8349B amplifier (20

dB gain) to give a viable measurement band of 2-18 GHz. By combining measurements from both bands, and using algorithms described in Section 2 to scale, splice and extrapolate the spectrum, an equivalent measurement bandwidth of 0-18 GHz is obtained.

The horn antennas are mounted within portholes cut into one wall of a 24x12x12 foot anechoic chamber which is lined with 6 inch pyramidal absorber. Scale model targets are placed on a low density foam pedestal mounted on an Arrick Robotics MD-2 Dual Stepper Motor computer controlled rotator located in the center of the chamber. The rotator is capable of 0.15 degree positioning accuracy from 0 to 360 degrees. At each aspect angle, the network analyzer acquires the data and sends it to a personal computer for processing and analysis.

A diagram of the measurement system is shown in Figure 1. As in any scattering system, the effects of the transmit/receive system transfer function, clutter, and target to chamber interactions must be removed to obtain accurate measurements. The calibration procedure is similar to that used by Morgan⁴ except that the initial raw measurements are performed in the frequency domain. The methodology is sufficiently different to merit a detailed description.

2.1. Calibration Procedure

The raw measured response of a target obtained with the anechoic chamber system differs from the actual response for two distinct reasons. First, the response of the measurement system (network analyzer, cables, amplifiers, antenna, propagation path) will modify the actual response through a convolution process. Second, there will be systematic errors introduced through reflections from the chamber walls (clutter) and interactions between the target and the chamber. Each of these effects is modeled in the measurement system diagram shown in Figure 2.

The first step in the calibration procedure is to make a background measurement of the empty chamber. This measured response is modelled as

$$R^b(f) = S(f) \{H_a(f) + H_c(f)\} + N^b(f) \quad (1)$$

where $H_a(f)$ describes the transfer function of the direct coupling from the transmit antenna to the receive antenna, $H_c(f)$ models the transfer function of the coupling from the transmit antenna to receive antenna via the anechoic chamber, antenna supports, and target mount, $N^b(f)$ is random noise and $S(f)$ is the system transfer function

$$S(f) = H_r(f) H_t(f) E(f) \quad (2)$$

Here $H_r(f)$ and $H_t(f)$ are the transfer functions of the receive and transmit antennas from the transmission line into the free-field environment while $E(f)$ represents the spectral content of the CW source.

Next, a calibration object with a known response is measured. For like-polarization measurements, a conducting sphere is used, with a known response calculated theoretically using the Mie series. For cross-polarization measurements, an inclined circular wire loop is used. This measurement gives

$$R^{c+b}(f) = S(f) \{H_a(f) + H_c(f) + H_s^c(f) + H_x^c(f)\} + N^{c+b}(f) \quad (3)$$

where $N^{c+b}(f)$ is random noise, $H_s^c(f)$ is the known transfer function of the calibration object, and $H_x^c(f)$ is the transfer function of the interaction of the calibration object with the anechoic chamber. Note that the interaction term is causal in the time domain; it cannot occur prior to the time required for the wave scattered from the target to reach the chamber walls and return to the receiving antenna. Note also that the interaction term is represented here as an additive effect.

The last measurement is of the target, giving

$$R^{t+b}(f) = S(f) \{H_a(f) + H_c(f) + H_t^t(f) + H_x^t(f)\} + N^{t+b}(f) \quad (4)$$

where $N^{t+b}(f)$ is random noise, $H_t^t(f)$ is the desired transfer function of the target and $H_x^t(f)$ is the transfer function due to the interaction of the target with the anechoic chamber. Again, this term is causal in the time domain.

Once these three measurements have been completed and stored in the computer, data processing to obtain the actual target scattered field response can be undertaken. First, the background measurement is subtracted from the measurements of the calibration object and the target. Subtracting (1) from (3) and (4) gives the clutter-free responses

$$\begin{aligned} R^c(f) &= S(f) \{H_s^c(f) + H_x^c(f)\} + N^c(f) \\ R^t(f) &= S(f) \{H_s^t(f) + H_x^t(f)\} + N^t(f) \end{aligned} \quad (5)$$

with the noise terms $N^c(f) = N^{c+b}(f) - N^b(f)$, $N^t(f) = N^{t+b}(f) - N^b(f)$. The next step in the calibration process depends on the quality of the anechoic chamber. If the anechoic chamber is of very high quality, then the interaction terms are small and can be neglected along with the noise terms giving

$$\begin{aligned} R^c(f) &= S(f)H_s^c(f) \\ R^t(f) &= S(f)H_s^t(f) \end{aligned} \quad (6)$$

Thus, the system transfer function can be determined from the know calibration response as

$$S(f) = \frac{R^c(f)}{H_s^c(f)} \quad (7)$$

Finally, the actual target response is given through

$$H_s^t(f) = \frac{R^t(f)}{S(f)} \quad (8)$$

For anechoic chambers of lesser quality, the interaction terms may be too large to be neglected. To solve this problem, $R^c(f)$ can be transformed to the time domain and time gating can be used to eliminate any interaction terms that are sufficiently delayed beyond the end of the calibration object response. Define the time response of the calibration measurement as

$$r^c(t) = \mathcal{F}^{-1}\{R^c(f)\} \quad (9)$$

Time gating with a window function $w(t)$ effectively excludes the interaction terms, giving

$$r^{cw}(t) = r^c(t)w(t) \quad (10)$$

Assuming that $w(t)$ excludes all of the interaction terms, and that $\mathcal{F}^{-1}\{S(f)H_s^c(f)\}$ is approximately time limited and not truncated by the window function, then

$$R^{cw}(f) = S(f)H_s^c(f) \quad (11)$$

where $R^{cw}(f) = \mathcal{F}\{r^{cw}(t)\}$. From this, the system transfer function $S(f)$ can be obtained as

$$S(f) = \frac{R^{cw}(f)}{H_s^c(f)} \quad (12)$$

Then, from (5)

$$H_s^t(f) + H_x^t(f) = \frac{R^t(f)}{S(f)} \quad (13)$$

Finally to isolate $H_s^t(f)$ the inverse Fourier transform is applied to obtain

$$H_s^t(t) + H_x^t(t) = \mathcal{F}^{-1}\left\{\frac{R^t(f)}{S(f)}\right\} \quad (14)$$

If the target response is approximately time limited, and the interaction term is causal and delayed beyond the end of the target

response, then the actual target response can be isolated using time gating to eliminate $H_x'(t)$.

To validate the calibration process, the response of a 0.0381 m diameter conducting sphere was measured using a 0.1778 m diameter sphere as a calibration object. The measured transfer function of the sphere is compared with its theoretical response in Figure 3 for the frequency band 2-18 GHz. Good agreement is seen throughout the band.

2.2 Splicing and extrapolation algorithm

If a target is measured within the two bands 0.4-7 and 2-18 GHz, the results can be combined to give an overall bandwidth of 0.4-18 GHz. It is found that if large scale model targets are used, good spatial resolution is obtained from the specular portion of the target response, but the major target resonances occur below 0.4 GHz. On the other hand, if a small target is used, the resonances are present but the spatial resolution is poor. This problem can be overcome by measuring a small target in the low frequency band and a larger version of the same target in the high frequency band. Assume the larger model, denoted A, has a scale of 1:A and the smaller model, denoted B, has a scale of 1:B. Then, frequency scaling for conducting targets allows the expression

$$R^A(f) = \left(\frac{B}{A}\right) R^B\left(\frac{A}{B}f\right) \quad (15)$$

where $R^A(f)$ and $R^B(f)$ are the measured responses of model A and B respectively. By using the above relation, $R^B(f)$ is converted to the same scale as model A. Thus, by combining both measurements, the response of the larger model is obtained within the effective bandwidth (0.4A/B-18 GHz). Typically, a ratio of 2:1 is used between the two targets, giving an equivalent frequency range of 0.2-18 GHz.

The splicing of the two target spectra $R^A(f)$ and $R^{BS}(f) = (B/A)R^B(fA/B)$ in a way that permits accurate determination of the transient response via the inverse FFT is somewhat difficult due to unavoidable phase differences between $R^A(f)$ and $R^{BS}(f)$. These phase differences are primarily due to variations in the effective range to models A and B. Any discontinuity in phase at the splicing frequency results in a non-causal, oscillatory signal being introduced into the transient response. A related problem arises from the abrupt termination of the band edges. If the data is inversely transformed into the time domain, oscillatory signals will again be introduced. The oscillation can be reduced by using an appropriate windowing function which tapers smoothly to zero at the band edges, but this will seriously reduce the presence of the low frequency resonances, resulting in a transient response with minimal late-time component.

To overcome these problems, $R^{BS}(f)$ is extrapolated to zero frequency with a linear phase, polynomial spectral function $R^E(f)e^{-j\alpha f}$, and then is multiplied by a progressive phase shift factor $\exp(-j\beta f)$. The optimal values of α and β are determined by minimizing the non-causal signal present before the beginning of the target response, t_0 . A genetic algorithm⁷ is used to minimize the energy

$$E = \int_{t_0-\Delta}^{t_0} [\mathcal{F}^{-1}\{W(f)(R^A(f) + [R^E(f)e^{-j\alpha f} + R^{BS}(f)]e^{-j\beta f})\}]^2 dt \quad (16)$$

where $W(f)$ is a weighting function which rolls off only at high frequency (typically a Gaussian function).

As an example, consider a B-58 model with scales of 1:48 and 1:96 measured at wing-on incidence with the electric field polarized in the plane of the aircraft. The spectral magnitude of the spliced and extrapolated spectral scattered field response is shown in Figure 4. There is clearly a low-frequency resonant region with sharp spectral peaks, followed by a high-frequency specular region. The inset shows an expanded version of the lower frequencies, showing the resonances and the extrapolation to zero frequency (using a function proportional to ω^2). Figure 5 shows the time-domain response obtained via the inverse FFT. Here there is a clear distinction between the early-time specular response, occurring as the incident field passes across the target, and the late-time resonant response. The solid line in Figure 5 is a result of using the genetic algorithm to minimize the oscillating precursor signal. If splicing is done without this minimization, the unacceptably poor

signal shown as the dotted line is obtained.

3. TRANSIENT DATA ANALYSIS AND VISUALIZATION

It is evident from the above description that several steps are required to obtain an ultrawide-band, transient target response. To minimize the required amount of human effort, the system has been automated to the greatest extent possible. At the beginning of each measurement process a calibration object and the empty chamber are measured, and the results transferred to a computer via an HPIB interface bus. A target is then placed upon a computer controlled rotatable platform, and the raw target response is automatically measured over a desired range of aspect angles with a step as fine as 0.15° . This data is sent to the computer and each set is processed to obtain a calibrated target response. The measurement process is repeated with a target of a different scale and the two sets of data are automatically spliced, extrapolated, and inverse transformed to give the final time-domain target responses.

A great deal of data can be rapidly accumulated for each target. To help understand the phenomenology of the scattering process, as is required before a successful target discrimination scheme can be developed, a significant effort must be put into analyzing the measured data. This encompasses two tasks: understanding the physics of the scattering process as a function of time, and understanding the dependence of the scattered field on aspect angle. To this end, several schemes have been developed to process the data and improve the visualization of the scattering effects.

Traditionally, the transient response of a radar target has been decomposed into two parts, an early-time specular response which occurs as the incident field waveform passes across the target, followed by a late-time natural mode response after the field has completely traversed the target. However, the measured data shows a more ambiguous delineation, complicated by the fact that small substructures may resonate during the period usually designated as early time, and global resonances may begin to be established before the onset of the late-time period. This effect can be observed quite clearly in Figure 6. Here the measured wing-on responses of 1:72 and 1:144 scale model B-52 aircraft have been combined together to obtain the short-pulse response. Overlaid with the response is the outline of the B-52. Clearly, there are specular reflections arising from the tip of the wing, the two engines, and the fuselage. Note also that the specular response is followed by a late-time natural mode response. However, an interesting effect is created by the shadowing of the leeward wing by the fuselage. There are no distinct specular reflections after the incident wave has passed the fuselage, but the natural mode series has obviously begun before the wave has completely passed the target. At this aspect angle, the natural response of the target is dominated by a fuselage resonance which begins to be established immediately after the incident wave has passed the fuselage. This is one instance of a natural response being imbedded within traditional early time. Examples of substructure resonances are also apparent. Plotted on the same graph is the transient response obtained using only the high-band (2-18 GHz) data. This data has no resonance information, which is easily seen by examining the difference between the curves in the late-time region. Note that there is also a difference following the specular reflection from the wing tip and from each engine. Since the difference is only due to low frequency information, there is a substructure resonance building after each specular reflection -- the resonances of the wingtip and the engines.

The confusing mixture of specular and resonant information can be sorted out and more easily visualized using a frequency-time plot. These plots have been used recently as a visual aid in many areas of electromagnetic scattering⁶. The plot is usually created by sliding a windowing function through the waveform and Fourier transforming the product of the waveform and the window. Often the window is allowed to expand as it moves (wavelet concept). For a narrow window, specular events are more evident; a wider window reveals resonant events. Since there is a combination of both types of events at many points within the target data, it is necessary to use a window with an adaptable window width. Figure 8 shows the plot generated using a rectangular window whose right side progresses uniformly in time through the waveform (shown at the bottom) and whose left side is allowed to expand at the same rate until either side encounters a large slope. At that point a specular reflection is detected and the width is reduced to a minimum value of 0.05 ns. When the window moves into a region of resonance, it expands to encompass the entire resonance until another specular reflection is encountered. The vertical axis is a plot of the spectrum within the window when the right side is at a given value of time (shown as the curve on the left for the largest time plotted). Specular reflections appear as dark stripes with wide bandwidth, while resonances appear as horizontal stripes. Thus, the substructure resonances are seen beginning to form after each specular reflection, and then finally progressing into two very strong body resonances in late time. This plot allows a visualization of the onset and behavior of both specular reflections and target resonances of all types.

Once there is an understanding of the complexity of each target response, it is not surprising that there are many ways to view the aspect dependence of the data. A very straightforward approach is to view the data as a three-dimensional plot of amplitude vs. aspect angle. This is shown in Figure 7 for the B-58 aircraft, measured from 0°-180° with a 0.9° step size. It is easily seen that both the early and late-time components are highly aspect dependent. By separating early and late times, more physical insight is provided. For instance, Figure 9 is a scattering plot showing the log amplitude of the response of the B-58 vs. aspect angle. Here the variation of the specular reflections are more easily seen. For example, at nose-on incidence (0°), the first reflection is from the nose, and later reflections come from the engine mounts, horizontal stabilizer, etc. As the aspect progresses toward wing-on (90°) the nose and tail reflection move inward to coincide with the fuselage, and the engine mounts move outward. This aspect dependent information can be accumulated and used to produce a spatial plot of an aircraft's specular points. For each spatial point (ρ', ϕ') an accumulation over aspect angles is given through

$$\pi(\rho', \phi') = \int_0^{2\pi} f\{[\rho - 2\rho'\cos(\phi' - \phi_i)]/c\} d\phi_i \quad (17)$$

where $[\rho - 2\rho'\cos(\phi' - \phi_i)]/c$ is the time delay to the point (ρ', ϕ') . Figure 10 shows the result for a 1:48 model TR-1, and an obvious image is created. Formula (17) is directly related to the time domain physical-optics imaging identity⁷.

Finally, the late-time data is most easily interpreted as a sum of body resonances with aspect independent natural frequencies and aspect dependent amplitudes and phases. By extracting these resonances using a genetic algorithm, a description of the aspect dependence is provided by plotting the variation of amplitude and phase vs. aspect angle. Figure 11 shows the modal amplitudes of the B-58 model. It is seen that the first dominant mode (perhaps a wing resonance) is very constant with aspect angle while the second mode (perhaps a fuselage resonance) shows a variation similar to thin wire structures.

4. ACKNOWLEDGEMENT

This work is supported by the Office of Naval Research under Grant No. N00014-93-1-1272.

5. REFERENCES

1. C. Phillips, P. Johnson, K. Garner, G. Smith, A. Shek, R.C. Chou and S. Leong, "Ultra-high-resolution radar development and test," in *Second Conference on Ultra-Wideband, Short-Pulse Electromagnetics*, New York, April 5-7, 1994.
2. Edward J. Rothwell, Kun-Mu Chen, Dennis P. Nyquist, Ponniah Ilavarasan, John E. Ross, Robert Bebermeyer, and Qing Li, "A general E-pulse scheme arising from the dual early-time/late-time behavior of radar scatterers," *IEEE Trans. on Ant. Propagat.*, vol. 42, no. 9, pp. 1336-1341, Sept. 1994.
3. J. Ross, P. Ilavarasan, E. Rothwell, R. Bebermeyer, K. M. Chen, D. Nyquist, and Q. Li, "Radar target discrimination using E-pulses with early-time and late-time responses," *IEEE AP-S International Symposium and URSI Radio Science Meeting*, Ann Arbor, MI, June 28-July 2, 1993.
4. M.A. Morgan, "Ultra-wideband impulse scattering measurements," *IEEE Trans. Ant. Propagat.*, vol. 42, no. 6, pp. 840-846, June 1994.
5. David E. Goldberg, *Genetic Algorithms*, Addison-Wesley, Reading, MA, 1989.
6. Lawrence Carin and Leopold B. Felsen, "Wave-oriented data processing for frequency- and time-domain scattering by nonuniform truncated arrays," *IEEE Antennas and Propagation Magazine*, vol. 36, no. 3, pp. 29-43, June 1994.
7. E.J. Rothwell, K.M. Chen, D.P. Nyquist and J.E. Ross, "Time-domain imaging of airborne targets using ultra-wideband or short-pulse radar," *IEEE Trans. Ant. Propagat.*, vol. 43, no. 3, pp. 327-329, March 1995.

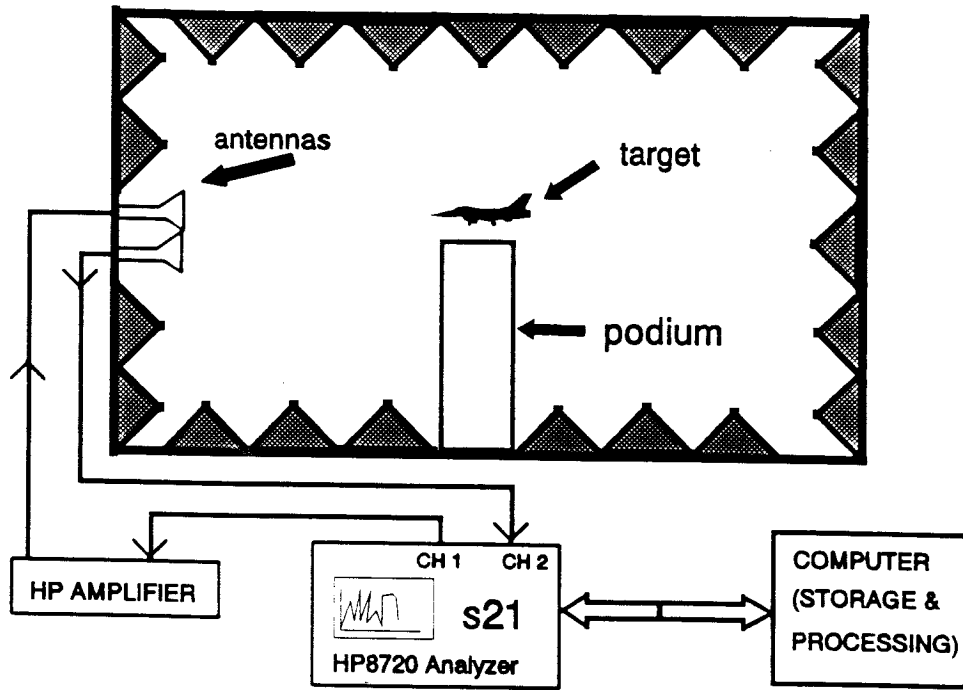


Figure 1. MSU ultrawide-band scattering range.

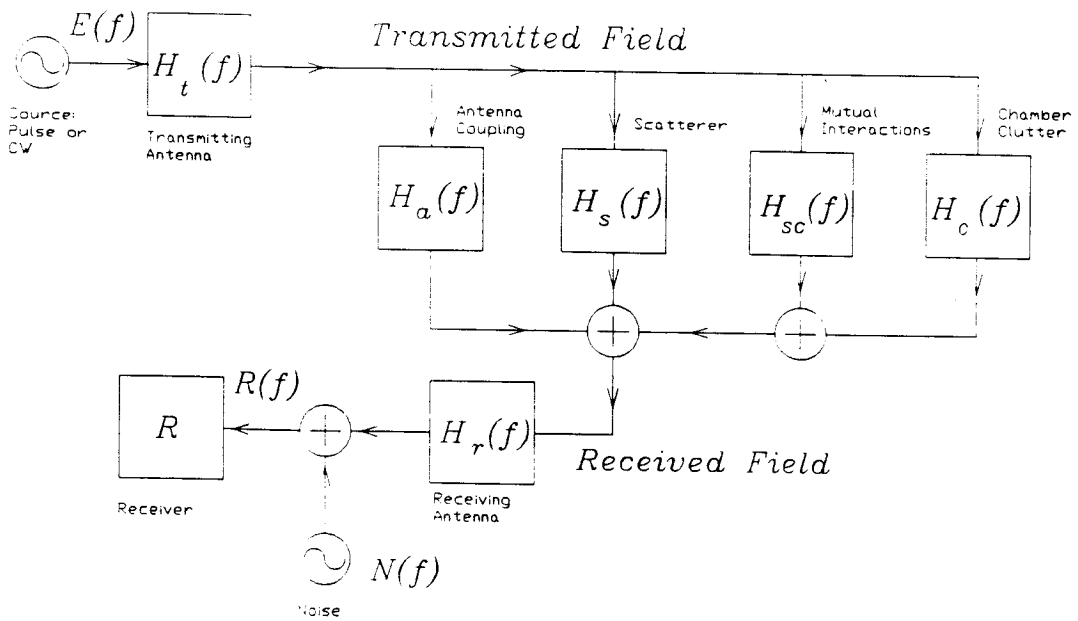


Figure 2. Block diagram model of measurement system.

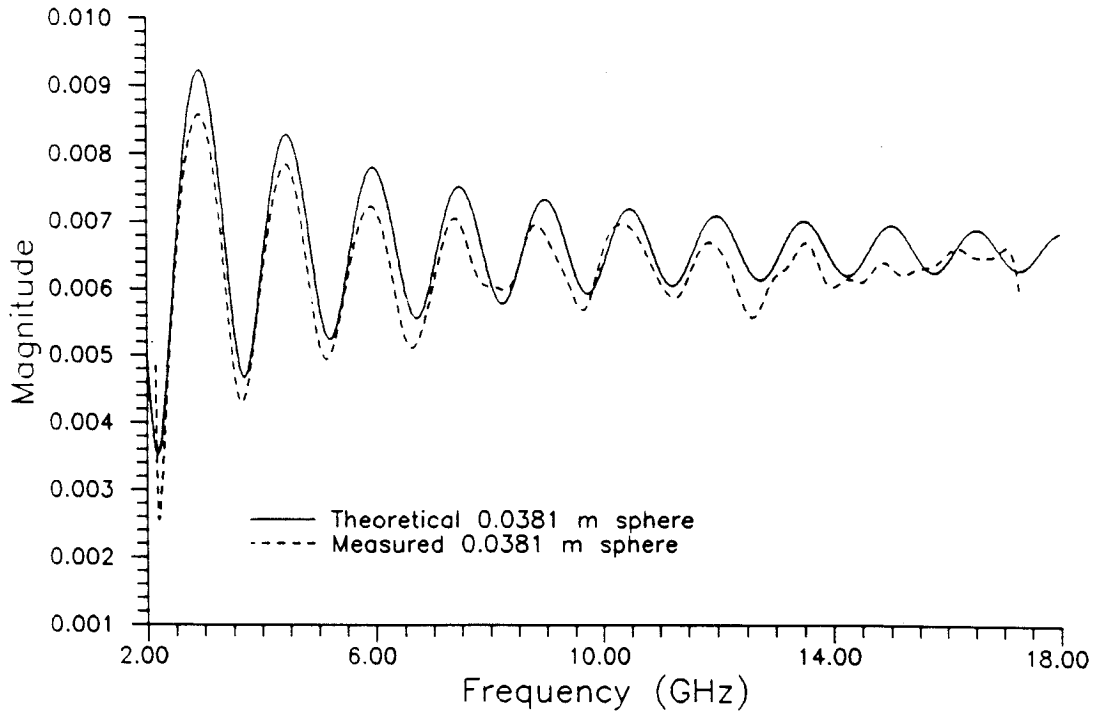


Figure 3. Measured response of 0.0381 m diameter conducting sphere, and comparison with theory.

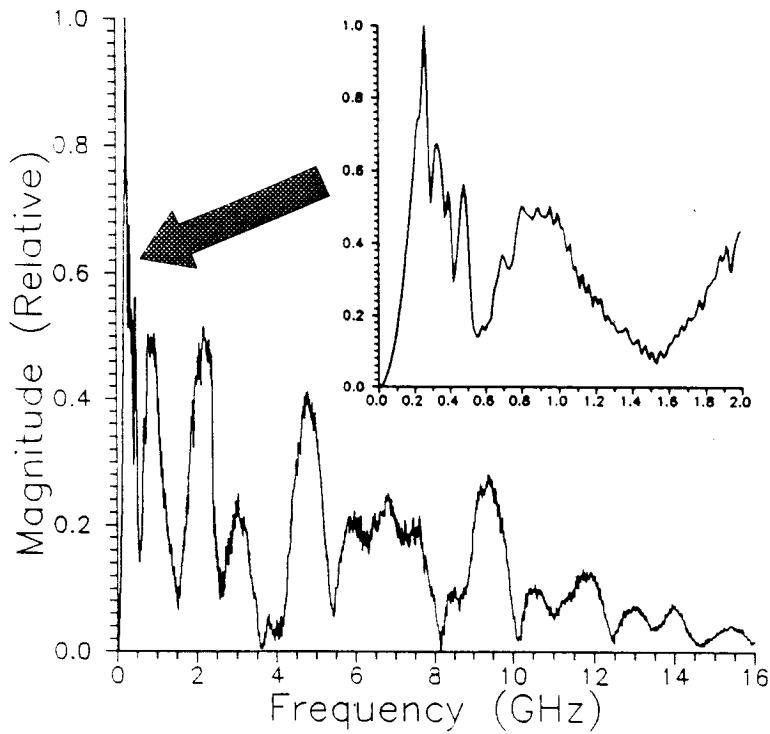


Figure 4. Spectral response of B-58 aircraft model. Inset shows expansion of low-frequency region. Wing-on (90°) incidence.

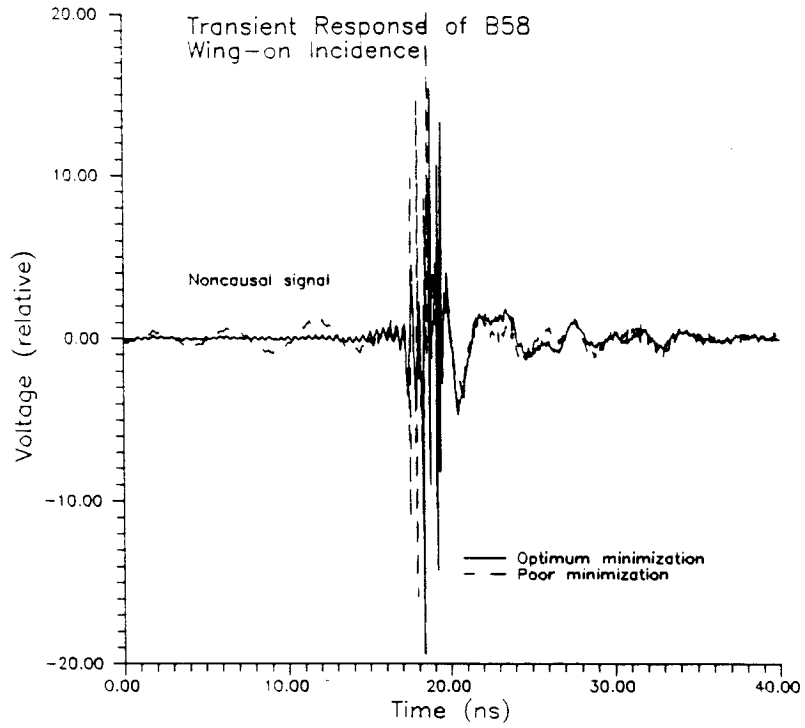


Figure 5. Transient response of B-58 showing early and late-time responses. Wing-on (90°) incidence.

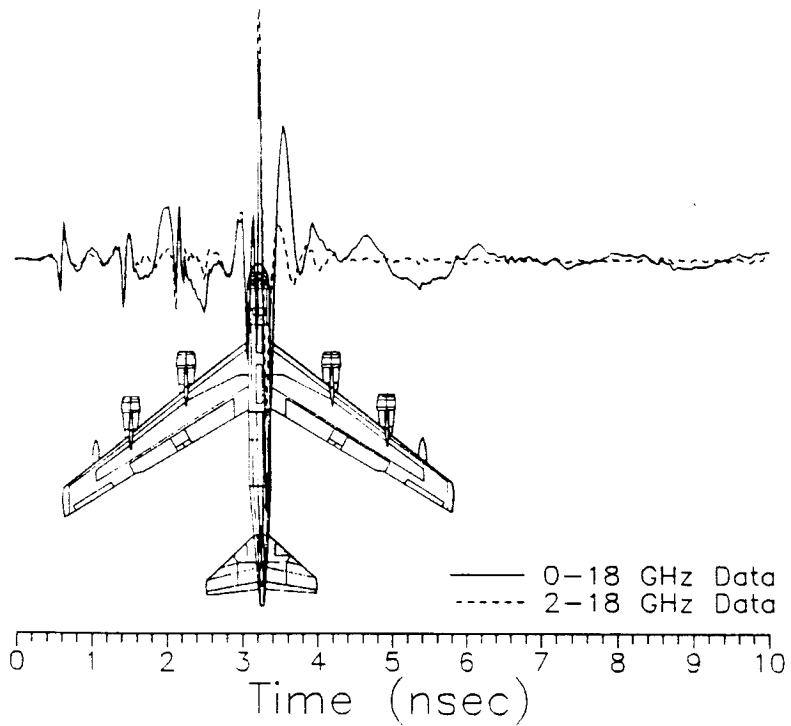


Figure 6. Transient response of B-52 showing specular reflections and substructure resonances. Wing-on (90°) incidence.

Transient Response synthesized from 2.18 GHz Data

b58b.dat

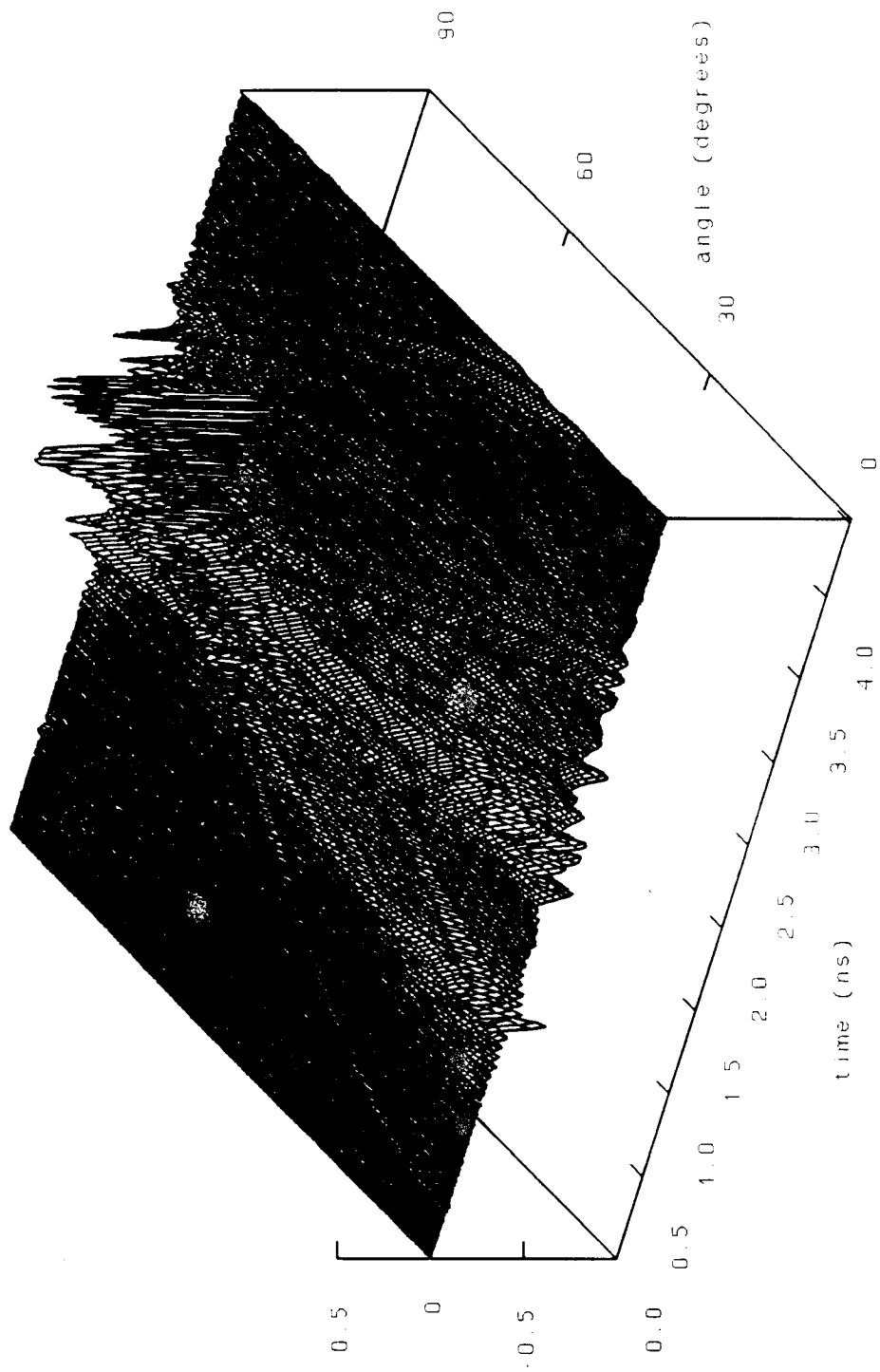


Figure 7. Transient response of B-58 as a function of aspect angle.

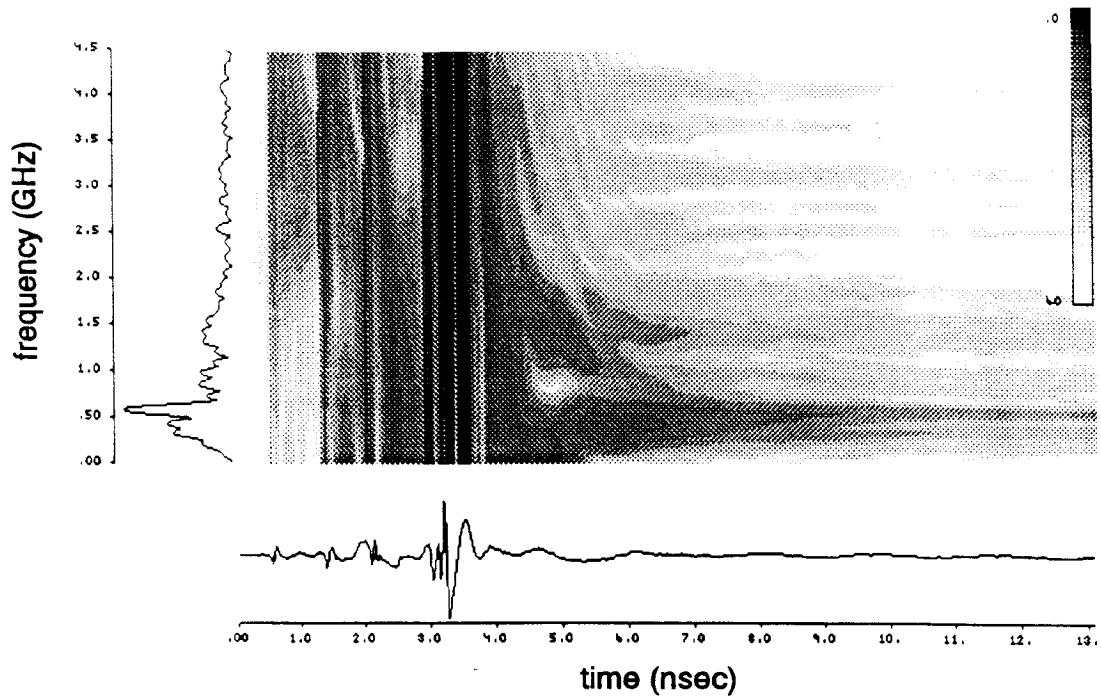


Figure 8. Frequency-time plot of transient B-52 response. Scale is in dB. Wing-on (90°) incidence.

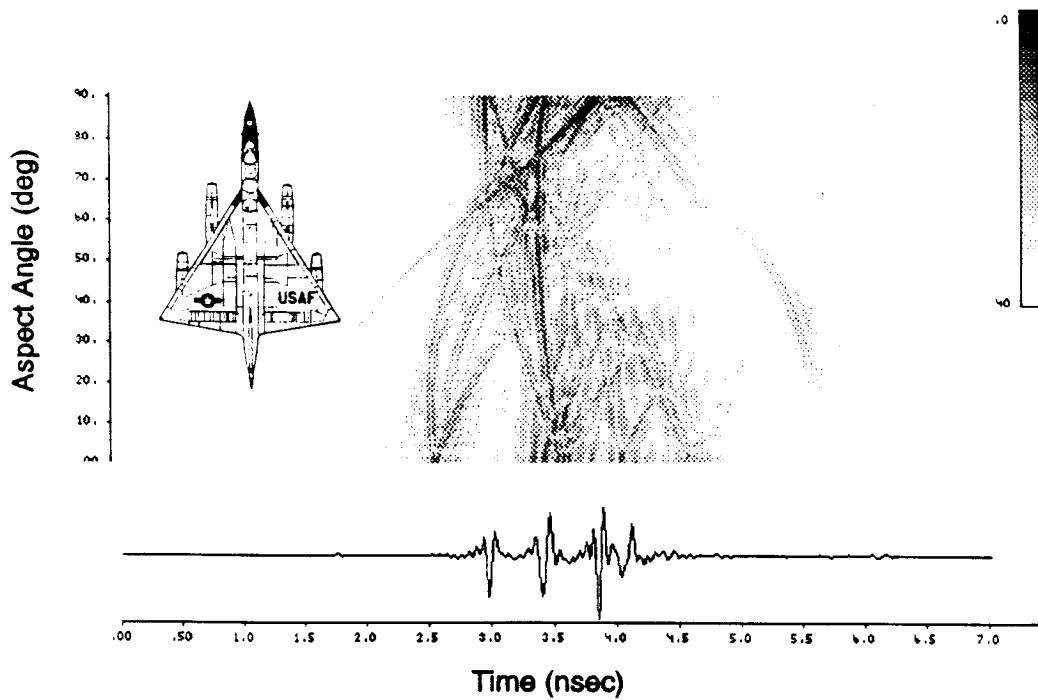


Figure 9. Scattering plot of B-58 showing variation of transient response with aspect angle. Scale is in dB.

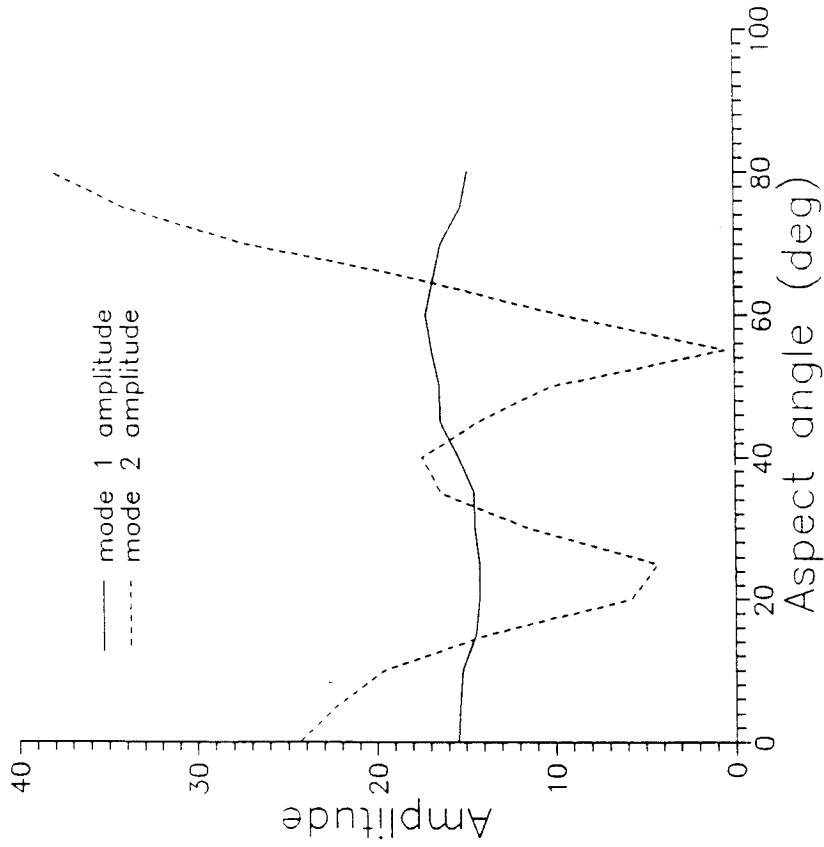


Figure 11. Variation in modal amplitudes of B-58 with aspect angle.

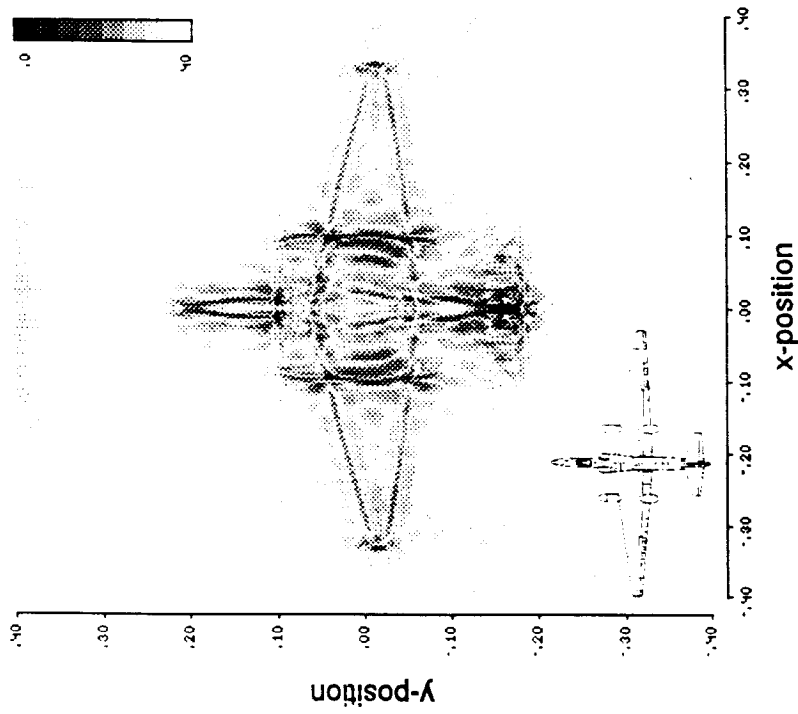


Figure 10. Image of TR-1. Scale is in dB.